

Flexible Indoor Localization and Tracking Based on a Wearable Platform and Sensor Data Fusion

Alessio Colombo, *Student Member, IEEE*, Daniele Fontanelli, *Member, IEEE*,
David Macii, *Member, IEEE*, and Luigi Palopoli, *Member, IEEE*

Abstract—Indoor localization and tracking of moving human targets is a task of recognized importance and difficulty. In this paper, we describe a position measurement technique based on the fusion of various sensor data collected using a wearable embedded platform. Since the accumulated measurement uncertainty affecting inertial data (especially due to the on-board accelerometer) usually makes the measured position values drift away quickly, a heuristic approach is used to keep velocity estimation uncertainty in the order of a few percent. As a result, unlike other solutions proposed in the literature, localization accuracy is good when the wearable platform is worn at the waist. Unbounded uncertainty growth is prevented by injecting the position values collected at a very low rate from the nodes of an external fixed infrastructure (e.g., based on cameras) into an extended Kalman filter. If the adjustment rate is in the order of several seconds and if such corrections are performed only when the user is detected to be in movement, the infrastructure remains idle most of time with evident benefits in terms of scalability. In fact, multiple platforms could work simultaneously in the same environment without saturating the communication channels.

Index Terms—Autonomous localization and mapping, Kalman filters, position measurement, uncertainty, wearable sensors, wireless sensor networks (WSNs).

I. INTRODUCTION

PEOPLE localization and, above all, tracking in indoor environments are notoriously challenging for various reasons [1]. First, the position accuracy requirements are generally stricter. Second, indoor environments are usually crowded and cluttered with other objects and obstacles, which hamper distance measurements. Finally, in many applications position tracking systems have to be noninvasive, i.e., small and wearable [2]. In addition, while in a positioning system just the location of a target in a certain area has to be determined sporadically or on demand, object tracking requires to measure position continuously and possibly in real-time. In the last years, many different solutions have been proposed

for indoor localization and tracking, but all of them suffer from important limitations. According to [3], none of the existing technologies can assure high performance and low cost, although a well-blended combination thereof can be a key factor of success. Moreover, the definition of the system performance as a baseline for a clear comparison among the different systems is very difficult and radically depends on users' needs, preference, and convenience. For example, in [4] five performance metrics are defined (i.e., accuracy, precision, complexity, robustness, and cost). The authors of [3] add to this set of metrics also security and privacy, user preference and availability. Moreover, in the case of tracking, real-time responsiveness and scalability (when multiple potential targets are in the same environment) are also of crucial importance for performance. The most accurate techniques for distance measurement and positioning are based on laser ultrasonic sensors [5], infrared (IR) sensors [6], rangefinders [7], video cameras [8], or a combination of them [9], [10]. The approach based on the measurement of the time-of-flight (ToF) of ultrasonic signals can be very accurate (i.e., in the order of a few centimeters) when a single target is considered [11], [12], but it is sensitive to the potential interference caused by other ultrasonic generators in the same area and often it is too power-hungry for wearable applications.

IR technology is used in the active badge system [13] (which has a room-level accuracy) and in the Firefly project [14] that can reach subcentimeter accuracy, but it is very expensive. The indoor global positioning system (iGPS) relies on triangulation of signals generated by IR emitters and guarantees a relatively high accuracy (in the order of a few centimeters [15]). However, it is very sensitive to external light and to line-of-sight (LOS) problems (which, instead, are very common in indoor environments).

The vision-based solutions are good for accurate indoor localization (they can estimate position with uncertainty in the order of a few centimeters) and they are quite omnidirectional [8], [16]. However, they are often sensitive to environmental light conditions and they are not scalable because of the computational workload incurred when several targets have to be tracked at the same time. Moreover, like the other optical-based techniques, also the solutions based on cameras can operate only in LOS conditions, which makes them impractical in applications where object tracking should rely on wearable devices.

One of the cheapest and simplest methods for localization and tracking is based on the measurement of the received radio signal power. In fact, the distance between a mobile

Manuscript received May 28, 2013; revised August 1, 2013; accepted September 8, 2013. Date of publication October 16, 2013; date of current version March 6, 2014. This work was supported in part by the European Union Seventh Framework Programme (FP7/2007-2013) under Grant ICT-2011-288917 Devices for Assisted Living and in part by the Autonomous Province of Trento, Trento, Italy, under Project Ambient Aware Assistance. The Associate Editor coordinating the review process was Dr. Antonios Tsourdos.

A. Colombo and L. Palopoli are with the Department of Information Engineering and Computer Science, University of Trento, Trento 38123, Italy (e-mail: colombo@disi.unitn.it; palopoli@disi.unitn.it).

D. Fontanelli and D. Macii are with the Department of Industrial Engineering, University of Trento, Trento 38123, Italy (e-mail: fontanelli@disi.unitn.it; david.macii@unitn.it).

Color versions of one or more of the figures in this paper are available online at <http://ieeexplore.ieee.org>.

Digital Object Identifier 10.1109/TIM.2013.2283546

device (e.g., worn by the user) and one or multiple anchor points can be estimated by inverting the relation between the received radio signal strength (RSS) and the distance from the transmitter, once the transmission power is known [17]. This approach relies on the RSS indicator integrated in most radio chips [18], and is very popular in the wireless sensor networks (WSNs) community [19], [20]. However, this technique is also strongly influenced by channel fading, multipath propagation, obstacles, and other non-stationary interferences [21], [22]. Performances can be improved (till reaching a standard uncertainty in the order of about 1 m), if RSS data are combined with the ToF values of exchanged radio messages [23]. Unfortunately, the ToF data can be subjected to large random fluctuations. Such fluctuations can be effectively reduced either through long averages over large data sets (at the cost of some delay) [24], or through low-level message timestamping (e.g., at the physical layer), possibly using special communication schemes such as ultra-wideband (UWB) pulses [25], [26], or chirp spread spectrum (CSS) signals [27], [28]. In this way, accuracies in the order of tens of centimeters or less, can be achieved. Nonetheless, the problem of handling the perturbations introduced by multiple objects in the environment still remains.

Localization based on the acquisition of signals from global navigation satellite systems (GNSS) is not possible without assisted global positioning systems [29], [30]. This approach generally assures just a rough localization in indoor environments (i.e., at the room level) because of the large attenuation of walls and roofs. An interesting alternative is offered by the Locata technology, which relies on a network of terrestrial and time-synchronized pseudolite transceivers (which can be used in connection or not with GNSS) [31]. This solution is similar to GPS in its general idea, but it works on a local scale, using the pseudolite transceivers. In particular, because of the high transmission power, positioning and tracking accuracy of tens of centimeters can be reached indoors [32]. This system is frequently used for structural monitoring [33] or aviation [34]. However, the antenna of the moving device is usually bulky and the receiver is quite power consuming, so it is not very suitable for wearable applications.

In conclusion, the qualitative analysis reported earlier confirms that indoor object tracking, at a low cost, with good accuracy and robustness in presence of obstacles and other possible users is still an open issue. It is our opinion that this problem can be solved only with careful tradeoffs at the design level, e.g., with wearable devices their own position can be reconstructed autonomously, with no or a little support from external infrastructures. A common approach of this type, especially in mobile robotics [35], is based on inertial platforms. Unfortunately, it is well known that the dynamic of a biped is much more complex than the dynamic of a wheeled vehicle. Therefore, when the inertial platform is worn by a human the unbounded uncertainty growth due to the accumulation of accelerometer and gyroscope noises is larger and less predictable than in vehicles, since it strongly depends on the specific features of human locomotion.

In the rest of this paper, at first, in Section II, an overview of the most known solutions based on inertial platforms for

human target localization and tracking are shortly summarized. Also, the main advantages of the proposed solution compared with other platforms are emphasized. In Section III, the theoretical background underlying the proposed algorithm is described, starting from the basic idea presented in [36]. Section IV provides a presentation of the developed wearable platform and the chosen experimental setup. Finally, in Section V several results collected on the field are reported and commented. Section VI concludes this paper.

II. INERTIAL SYSTEMS FOR INDOOR NAVIGATION

An inertial platform, sometimes referred to also as an inertial navigation system (INS) or inertial measurement unit (IMU), consists of multiple sensors (particularly gyroscopes, accelerometers, and compasses) and it can be used to measure the distance covered by a moving object in a given reference frame. As known, an INS is ideally autonomous, as it does not require any external intervention. However, purely inertial solutions for localization are affected by unavoidable position uncertainty growth [37], [38]. In outdoor vehicles such as land crafts, aircrafts, and ships, position can be estimated by combining inertial sensor data with GPS coordinates. A well-known example is the so-called dead-reckoning, a technique whereby automotive navigators can compensate for the absence of satellite information by using accelerometers or encoders on the wheels. A similar approach has been extended also to personal navigation systems [39], but it can be hardly used indoors. Moreover, the acceleration profile of a walking pedestrian is radically different from that of a vehicle, the latter being generally smoother and more regular. In addition, the estimation of the tangential acceleration component along the trajectory is much noisier, since it depends on the platform attitude that can change over time in three dimensions. Some researchers tried to tackle this problem by means of an external wireless infrastructure, e.g., through radio beacons [40], or by combining multiple techniques using a Bayesian recursive estimation algorithm [41]. In [42], the authors suggest that the position error drift can be avoided if the inertial platform is fastened to one shoe. Indeed, feet stop briefly on the ground in between steps. During these short breaks, the actual instantaneous foot velocity is zero. Therefore, a technique typically known as zero velocity update can be used to correct possible residual velocity errors anytime a step is detected. Two variants of the same basic idea are described in [43] and [44]. In both cases, uncertainty is in the order of a fraction of percent of the total walking distance. The main drawback of this method is that it is not always possible or comfortable to wear an electronic device on one foot (e.g., when disabled or elderly people have some deambulation problem). Also, it looks more suitable for outdoor pedestrian tracking than for indoor navigation. To overcome these limitations, the platform described in this paper is conceived to be worn on the trunk (e.g., on a belt around the waist), since the trunk is considered as the best frame to account for the nonholonomic nature of human locomotion [45]. To avoid unbounded uncertainty growth, the coordinates measured periodically by an external infrastructure (e.g., based on radio anchor points [44],

smart cameras [46], or microphones [47], [48]) are used to adjust the position estimated by the platform at a very low rate (in the order of several seconds).

The proposed approach results from the evolution of the solution preliminarily presented in [36]. In fact, both accuracy and precision of that implementation were strongly affected by user velocity estimation drift. This problem was tackled by updating the user position from the external infrastructure quite frequently (i.e., every 1–5 s). The new technique removes this limitation and relaxes the update period, thus making the system much more autonomous than the previous one. Since the loss of accuracy in open-loop conditions (namely without external updates) is now about one order of magnitude smaller, position tracking uncertainty can be lower than 50 cm even after several seconds of continuous motion. In particular, compared with [36], the following significant improvements have been introduced:

- 1) A nonlinear filter based on an original heuristic step detection algorithm is used to remove the spurious velocity errors resulting from the integration of acceleration noise in between subsequent steps.
- 2) Yaw angle estimation is improved by means of a specific stretching algorithm that relies on two consecutive external position estimates.
- 3) Better sensors have been integrated in a totally new, low-cost wearable embedded platform.

Last, but not least, the experiments were conducted in a properly instrumented environment to evaluate system performances with better accuracy. Ultimately, the advantages of the proposed approach are: 1) enhanced scalability; 2) flexible tradeoff between cost, expected accuracy and adjustment rate; and 3) ability of tracking a person temporarily even when he/she moves in areas that are not covered by the fixed monitoring infrastructure.

III. MEASUREMENT TECHNIQUE

A. Overview

Let $\langle W \rangle$ be a right-handed global (or world) reference frame defined by axes X_w , Y_w and Z_w with X_w pointing toward north and Z_w directed as the gravity acceleration vector. Let $\langle R \rangle$ and $\langle U \rangle$ be two additional right-handed relative Cartesian frames defined by axes X_r , Y_r , Z_r and X_u , Y_u , Z_u , respectively. Frame $\langle R \rangle$ is attached to an inertial platform equipped with a three-axis accelerometer, a three-axis gyroscope measuring the angular velocities of the platform around the axes of $\langle R \rangle$ and a three-axis magnetometer working as a compass (i.e., pointing to the same direction as X_w). Of course, frame $\langle R \rangle$ is rotated with respect $\langle W \rangle$ and its attitude generally changes over time.

Frame $\langle U \rangle$ refers to the trajectory of the user wearing the platform. This means that X_u is tangential to the trajectory of the moving body, Z_u coincides with Z_w and finally the direction of Y_u is given by the right-hand rule. Thus, the user frame has the plane $X_u \times Y_u$ parallel to $X_w \times Y_w$, but the yaw angle between X_u and X_w changes over time. A qualitative representation of the three reference frames mentioned earlier is sketched in Fig. 1. As shown in Fig. 2, the position estimation technique basically consists of the following:

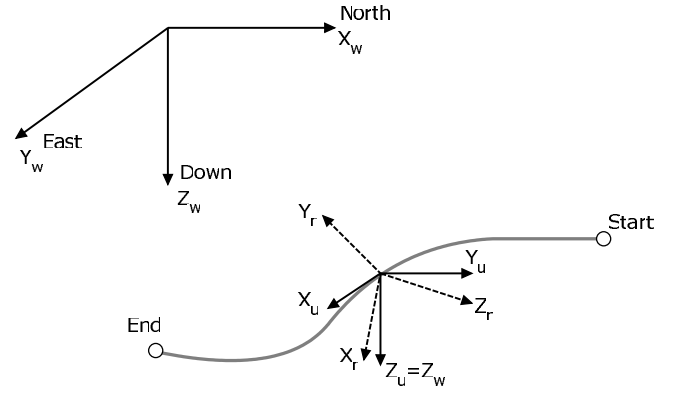


Fig. 1. Relative frame to world frame rotation.

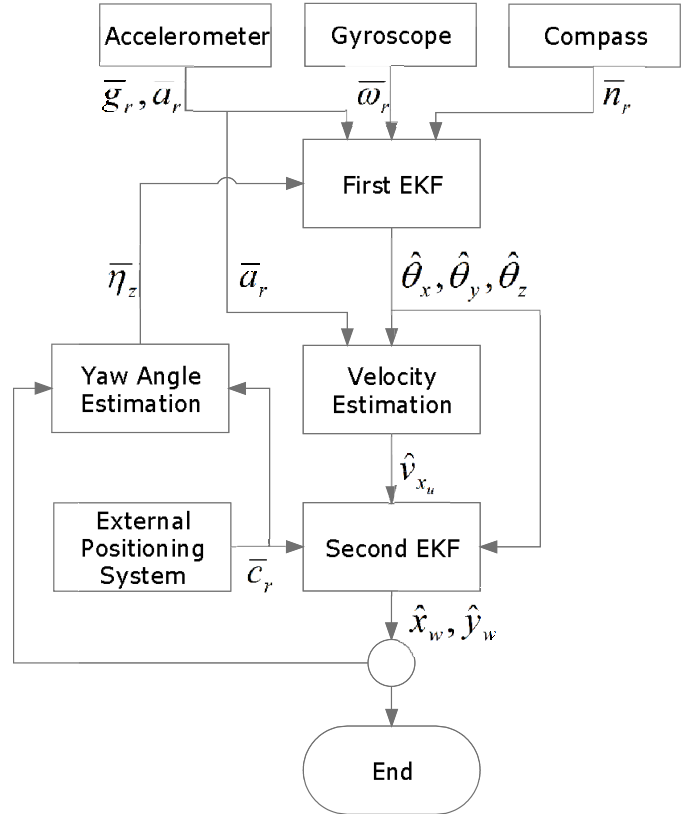


Fig. 2. Block diagram of the position estimation algorithm.

- 1) two cascaded extended Kalman filters (EKFs) processing the inertial data;
- 2) an algorithm based on a hybrid automaton estimating the target velocity along X_u and removing the drift due to the oscillatory behavior of biped motion;
- 3) an external infrastructure measuring the position of the user in the global reference frame;
- 4) an algorithm improving yaw angle estimation accuracy, since compass-based direction measurements in indoor environments can be strongly perturbed by the presence of materials distorting Earth's magnetic field.

It is worth emphasizing that even if the general idea still relies on two EKFs as described in [36], the overall estimation

algorithm is different, because in that version the velocity drift was only partially removed by the second EKF and no additional attitude corrections were considered. In this new version, the presence of two additional observers (i.e., for user velocity and yaw angle, respectively) taking into account the dynamic of human locomotion, increases robustness and accuracy of the proposed technique. For the sake of clarity, the following notation will be used throughout this paper: the symbols topped with a bar (e.g., $\bar{\theta}_z$) represent the measurement results directly collected from sensors, while the hatted symbols (e.g., $\hat{\theta}_z$) refer to the values estimated indirectly through some algorithm (e.g., a Kalman filter). If not otherwise specified, the symbols without special additional marks just refer to the corresponding quantities to be measured. In the following sections, the operation of any of the functional blocks shortly described earlier is analyzed in detail.

B. First EKF: Attitude Estimation

The first EKF estimates the attitude of $\langle R \rangle$ with respect to $\langle W \rangle$. Attitude is described by means of three angles, i.e., the roll θ_x , the pitch θ_y , and the yaw θ_z , which can be combined in the vector $\boldsymbol{\theta} = [\theta_x, \theta_y, \theta_z]^T$. The nonlinear system modeling the attitude dynamics is [36]

$$\begin{cases} \dot{\boldsymbol{\theta}} = E(\boldsymbol{\theta})\boldsymbol{\omega}_r \\ \mathbf{g}_r = R_{zyx}(\boldsymbol{\theta})^T \mathbf{g}_w \\ \mathbf{n}_r = R_{zyx}(\boldsymbol{\theta})^T \mathbf{n}_w \\ \eta_z = C\boldsymbol{\theta} \end{cases} \quad (1)$$

where $\boldsymbol{\omega}_r = [\omega_{x_r}, \omega_{y_r}, \omega_{z_r}]^T$ is the vector of the angular velocities (which can be measured by a gyroscope), $\mathbf{g}_w = [0, 0, 9.8]^T$ m/s² and $\mathbf{n}_w = [1, 0, 0]^T$ are the gravity acceleration vector and the north-directed unit vector in the global frame $\langle W \rangle$, \mathbf{g}_r , and \mathbf{n}_r are the same vectors in $\langle R \rangle$

$$E(\boldsymbol{\theta}) = - \begin{bmatrix} 1 & \sin \theta_x \tan \theta_y & \cos \theta_x \tan \theta_y \\ 0 & \cos \theta_x & -\sin \theta_x \\ 0 & \frac{\sin \theta_x}{\cos \theta_y} & \frac{\cos \theta_x}{\cos \theta_y} \end{bmatrix} \quad (2)$$

is the system matrix mapping the angular velocities of the platform into the time derivatives of the angles $\boldsymbol{\theta}$, $C = [0, 0, 1]$ is the output matrix and $R_{zyx}(\boldsymbol{\theta})$ is the total rotation matrix of frame $\langle R \rangle$ with respect to frame $\langle W \rangle$. The details about the derivation of expression (2) and $R_{zyx}(\boldsymbol{\theta})$ are reported in the Appendix A. Rotation matrices belong to the Special Orthogonal Group SO(3), for which the general property $R_{zyx}^T = R_{zyx}^{-1}$ holds. If the sampling period T_c of all inertial sensors is the same, the discretized version of (1) is

$$\begin{cases} \boldsymbol{\theta}(k+1) = \boldsymbol{\theta}(k) + T_c E[\boldsymbol{\theta}(k)]\boldsymbol{\omega}_r(k) \\ \mathbf{o}_r(k) = U[\boldsymbol{\theta}(k)]\mathbf{o}_w(k) \end{cases} \quad (3)$$

where $\boldsymbol{\theta}(k)$ is the state of the system at time $t_k = kT_c$, $\mathbf{o}_w = [\mathbf{g}_w^T(k), \mathbf{n}_w^T(k), \theta_z(k)]^T$, $\mathbf{o}_r = [\mathbf{g}_r^T(k), \mathbf{n}_r^T(k), \eta_z(k)]^T$, and

$$U[\boldsymbol{\theta}(k)] = \begin{bmatrix} R_{zyx}[\boldsymbol{\theta}(k)]^T & 0_{3,3} & 0_{3,1} \\ 0_{3,3} & R_{zyx}[\boldsymbol{\theta}(k)]^T & 0_{3,1} \\ 0_{1,3} & 0_{1,3} & 1 \end{bmatrix} \quad (4)$$

is the output matrix (which also depends on the state of the system), with $0_{i,j}$ being a $i \times j$ all-zeros matrix. The state of (3) can be estimated by means of an EKF resulting from the linearization of (1) and from the measurement of $\boldsymbol{\omega}_r(k)$, $\mathbf{g}_r(k)$, $\mathbf{n}_r(k)$, and $\eta_z(k)$, supposing that the uncertainty contributions affecting such quantities are non-stationary, white and normally distributed. In a first approximation, if sensors are preliminarily calibrated, this assumption is reasonable because the fluctuations affecting the quantities above result from the superimposition of the intrinsic vibrations of the platform and the measurement uncertainty of the sensors employed.

In the prediction step of the EKF, the predicted state is given by [36]

$$\boldsymbol{\theta}^+(k+1) = \hat{\boldsymbol{\theta}}(k) + T_c E[\hat{\boldsymbol{\theta}}(k)]\bar{\boldsymbol{\omega}}_r(k) \quad (5)$$

where $\hat{\boldsymbol{\theta}}(k)$ is the state estimated at time t_k and $\bar{\boldsymbol{\omega}}_r(k)$ is the vector including the angular velocity components measured by the gyroscope at the same time. Similarly, the predicted state covariance matrix $P_\theta(k)$ results from

$$P_\theta^+(k+1) = F_\theta(k)P_\theta(k)F_\theta^T(k) + G_\omega(k)Q_\omega(k)G_\omega^T(k) \quad (6)$$

where:

- 1) $F_\theta(k) = I_3 + T_c \partial(E(\boldsymbol{\theta})\boldsymbol{\omega}_r)/\partial\boldsymbol{\theta}|_{[\hat{\boldsymbol{\theta}}(k), \bar{\boldsymbol{\omega}}_r(k)]}$ is the Jacobian of the system matrix with respect to the state vector $\boldsymbol{\theta}$ computed at $[\hat{\boldsymbol{\theta}}(k), \bar{\boldsymbol{\omega}}_r(k)]$ and I_3 is the 3×3 identity matrix;
- 2) $G_\omega(k) = T_c \partial(E(\boldsymbol{\theta})\boldsymbol{\omega}_r)/\partial\boldsymbol{\omega}_r|_{[\hat{\boldsymbol{\theta}}(k), \bar{\boldsymbol{\omega}}_r(k)]} = T_c E[\hat{\boldsymbol{\theta}}(k)]$ is the Jacobian of the system matrix with respect to the input velocity vector $\boldsymbol{\omega}_r$ computed at $[\hat{\boldsymbol{\theta}}(k), \bar{\boldsymbol{\omega}}_r(k)]$;
- 3) $Q_\omega(k)$ is the covariance matrix associated with $\bar{\boldsymbol{\omega}}_r(k)$ including both intrinsic and measurement uncertainty contributions.

Also, the measurement prediction equation of the EKF is

$$\mathbf{o}_r^+(k+1) = U[\boldsymbol{\theta}^+(k+1)]\mathbf{o}_w(k+1). \quad (7)$$

In the update step of the EKF, the predicted values $\boldsymbol{\theta}^+(k+1)$ and $P_\theta^+(k+1)$ are updated using the available measurement results. Thus, the attitude update equation is

$$\hat{\boldsymbol{\theta}}(k+1) = \boldsymbol{\theta}^+(k+1) + K_\theta(k+1)\bar{\mathbf{o}}_r(k+1) \quad (8)$$

where $\bar{\mathbf{o}}_r(k+1) = \mathbf{o}_r(k+1) - \mathbf{o}_r^+(k+1)$ is the innovation term at time t_{k+1}

$$K_\theta(k+1) = P_\theta^+(k+1)H_\theta^T(k+1) \cdot [H_\theta(k+1)P_\theta^+(k+1)H_\theta^T(k+1) + Q_o(k+1)]^{-1} \quad (9)$$

is the Kalman gain, $H_\theta(k+1) = \partial U(\boldsymbol{\theta})\mathbf{o}_w/\partial\boldsymbol{\theta}|_{\boldsymbol{\theta}^+(k+1)}$ and finally

$$Q_o(k+1) = \begin{bmatrix} Q_g(k+1) & 0_{3,3} & 0_{3,1} \\ 0_{3,3} & Q_n(k+1) & 0_{3,1} \\ 0_{1,3} & 0_{1,3} & Q_\eta(k+1) \end{bmatrix} \quad (10)$$

is the covariance matrix of the measurement result vector $\bar{\mathbf{o}}_r(k+1) = [\bar{\mathbf{g}}_r^T(k+1), \bar{\mathbf{n}}_r^T(k+1), \bar{\eta}_z(k+1)]^T$ at time t_{k+1} . Observe that (10) is a block diagonal matrix because the covariance matrices associated with $\bar{\mathbf{g}}_r(k)$, $\bar{\mathbf{n}}_r(k)$, and $\bar{\eta}_z$ are uncorrelated. Term $\bar{\eta}_z(k+1)$ deserves a special attention. In fact, when the angle values result from the algorithm described in Section III-E, we have that $\bar{\eta}_z(k+1) = \bar{\theta}_z(k+1)$.

However, since the infrastructure is supposed to operate at a very low rate, we generally have that this measure is not available. In such cases, the last row and column of matrices (4) and (10) are removed, the linearized output matrix H also changes accordingly, and finally the update step of the EKF just relies on the data coming from the accelerometer and the magnetometer. As a result, the attitude covariance matrix update equation is

$$P_\theta(k+1) = [I_3 - K_\theta(k+1)H(k+1)]P_\theta^+(k+1). \quad (11)$$

C. User Velocity Estimation

If both the attitude angles and the acceleration components of the moving body in $\langle R \rangle$ are known with a negligible uncertainty, the acceleration components in the user frame $\langle U \rangle$, i.e., $\mathbf{a}_u = [a_{x_u}, a_{y_u}, a_{z_u}]^T$ result from

$$\mathbf{a}_u = R_y(\theta_y)R_x(\theta_x)\mathbf{a}_r \quad (12)$$

and the tangential velocity component of the moving user in $\langle U \rangle$ is simply given by the integral of a_{x_u} . Unfortunately, it is known that the velocity values obtained with this approach tend to drift over time due to the accumulation of multiple uncertainty contributions associated with the respective measured quantities $\hat{\mathbf{a}}_u$, $\hat{\theta}_x$, and $\hat{\theta}_y$, which cause severe positioning errors. Nonetheless, several experiments on the field showed that [36]: 1) in indoor environments people stop and go frequently and 2) the most significant acceleration and deceleration components in “natural” walking conditions occur at the beginning and at the end of each movement, respectively. During motion instead, the user velocity is generally quite constant and the tangential acceleration patterns exhibit a clear alternate behavior due to the typical sequence of steps of biped locomotion [49]. Of course, the integral of each pair of alternate (i.e., positive/negative) acceleration waveforms is not exactly zero, since the body of the user does not stop completely in between steps. However, if the intrinsic velocity variations are low enough to be comparable with the accumulated noise introduced by the accelerometer, they can be filtered with no serious consequences in terms of accuracy. The velocity estimation algorithm described in the following relies on the observations above and it assures good performance under the assumption that the user motion is quite regular, that is, quite continuous without large accelerations and decelerations except those related to users’ intermediate stops. The algorithm can be formally described by the hybrid automaton depicted in Fig. 3. The automaton is defined by the tuple $\mathcal{H} = (\Xi, \Xi_0, \Sigma, \Lambda, \Delta, R)$, where:

- 1) $\Xi = \Gamma \times S$ is the hybrid state space. In particular, the proposed automaton has three discrete states $\Gamma = \{\gamma_0, \gamma_1, \gamma_2\}$: γ_0 corresponds to no motion, while γ_1 and γ_2 correspond to the accelerated motion and the decelerated motion, respectively, caused by one step. Therefore, each hybrid state is described by the automaton discrete state γ_i and by the dynamic state variable $x_s(k) = [\delta_v(k), v_{x_u}(k)]^T \in S$, where $\delta_v(k)$ is the increment in velocity during a single step at time t_k and $v_{x_u}(k)$ is the tangential user velocity in frame $\langle U \rangle$.

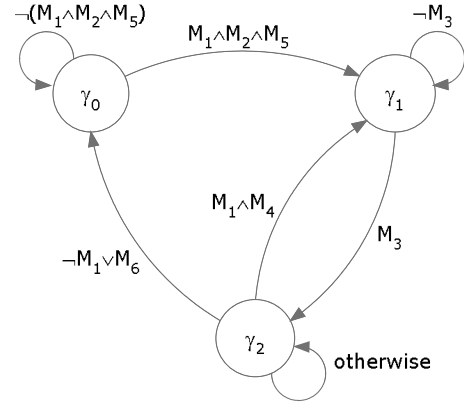


Fig. 3. Hybrid automaton driving the heuristic to estimate velocity.

Notice that $\delta_v(k)$ has to be reset in between subsequent steps.

- 2) $\Xi_0 = (\gamma_0, x_s(0))$ is the initial state of the hybrid automaton, with $x_s(0) = [0, 0]^T$.
- 3) Σ is the set of dynamic systems associated with the states of Γ . Each state γ_i is described by a linear system of the form $x_s(k+1) = A(\gamma_i)x_s(k) + B(\gamma_i)a_{x_u}(k)$. In particular, $A(\gamma_0) = 0_{2,2}$ and $B(\gamma_0) = 0_{2,1}$, $A(\gamma_1) = A(\gamma_2) = I_2$, and $B(\gamma_1) = B(\gamma_2) = T_c \mathbf{1}_2$, where T_c is the sample period of inertial signals (as specified in the previous sections) and $\mathbf{1}_n$ is an all-one column vector of dimension n .
- 4) $\Lambda = \Gamma \times \Gamma$ is the collection of graph edges depicted in Fig. 3.
- 5) $\Delta : \Lambda \rightarrow \{M_1, M_2, M_3, M_4, M_5\}$ maps each edge to its guard set.
 - a) M_1 is true if and only if the estimated standard deviation $\hat{\sigma}_{a_{x_u}}$ of a_{x_u} over a window of duration T_m (e.g., 0.5 s) is greater than a given threshold $\sigma_{a_{\min}}$. In practice, this parameter leverages between motion detection sensitivity and effect of accelerometer noise. The higher the value of $\sigma_{a_{\min}}$, the stiffer the algorithm is in detecting human motion. On the other hand, the lower the value of $\sigma_{a_{\min}}$, the more sensitive the algorithm becomes in detecting user motion. It was observed experimentally that $\sigma_{a_{\min}} = 0.2 \text{ m/s}^2$ assures a good tradeoff between sensitivity and accuracy.
 - b) M_2 is true if and only if the time spent in γ_0 is at least equal to T_m . This parameter is used to prevent spurious transitions through state γ_0 between subsequent steps.
 - c) M_3 is true if and only if the acceleration pattern $a_{x_u}(k)$ crosses zero with a negative slope at time t_k .
 - d) Dually, M_4 is true if and only if the acceleration pattern $a_{x_u}(k)$ crosses zero with a positive slope at time t_k .
 - e) M_5 is true if and only if $a_{x_u}(k) > 0$.
 - f) Finally, M_6 is true if and only if $v_{x_u}(k)$ changes its sign at time t_k . Condition M_6 is needed to remove sudden, erroneous velocity variations occurring during one step (e.g., due to body posture changes).

The transitions between pairs of states of the hybrid automaton \mathcal{H} are fired on the basis of Λ with period T_c . The set of logical relationships firing all possible transitions is again shown in Fig. 3.

- 6) $R : \Lambda \rightarrow S$ is the reset map for each state transition defined in the edge set Λ . In general, $x_s(k)$ does not change within a given state. However, on edge (γ_2, γ_1) the following expression holds:

$$R(\gamma_2, \gamma_1) = \begin{bmatrix} 0 \\ \rho_{21}(k) \end{bmatrix} \quad (13)$$

where

$$\rho_{21}(k) = \begin{cases} v_{xu}(k), & \text{in the first 2 steps} \\ v_{xu}(k) - \delta_v(k), & \text{afterward.} \end{cases} \quad (14)$$

In essence, this means that during any transition from γ_2 to γ_1 (i.e., at the end of each step and just before a new step begins):

- The velocity increment related to the last step is reset.
- This increment is considered to be a part of user velocity only in the first two steps, whereas it is removed afterward (i.e., till the user stops again) to prevent spurious velocity drifts due to the accumulated uncertainty.

The heuristic criterion mentioned above relies on the considerations reported at the beginning of this section and it is justified by the fact that in practice after two steps the velocity of the user in “natural” walking conditions usually reaches a steady state. In the following, since the actual velocity values depend on the estimated quantities $\hat{\mathbf{a}}_u$, $\hat{\theta}_x$, and $\hat{\theta}_y$, the output of the algorithm is an estimated quantity as well. Therefore, it will be denoted as \hat{v}_{xu} in the following.

D. Second EKF: Position Estimation

Assuming that:

- users move just on a plane (i.e., $v_{zu} \approx 0$);
- left/right body translations are negligible (i.e., $v_{yu} \approx 0$ because of the nonholonomic nature of the human locomotion [45]);
- user tangential velocity v_{xu} is known;

then the position of the target in $\langle W \rangle$ is simply given by [36]

$$\begin{cases} \dot{\mathbf{p}} = \mathbf{s}(\theta_z)v_{xu} \\ \mathbf{c} = \mathbf{p} \end{cases} \quad (15)$$

where $\mathbf{s}(\theta_z) = [\cos \theta_z, \sin \theta_z]^T$. In practice, however, the values of v_{xu} result from the velocity estimation algorithm reported in Section III-C, while the yaw angles θ_z are estimated by the first EKF. Since both quantities are sampled with the same period T_c and are affected by both intrinsic fluctuations and measurement uncertainty contributions, the state of the discretized version of (15) can be estimated by another EKF. In particular, the state prediction equation for a given input vector $[\hat{\theta}_z(k), \hat{v}_{xu}(k)]^T$ is

$$\mathbf{p}^+(k+1) = \hat{\mathbf{p}}(k) + T_c \mathbf{s}[\hat{\theta}_z(k)] \hat{v}_{xu}(k) \quad (16)$$

where $\hat{\mathbf{p}}(k)$ is the estimated state at time t_k . Similarly, the state prediction covariance matrix results from the linearization and discretization of (15) and it is given by

$$P_p^+(k+1) = P_p(k) + G_\theta(k) \sigma_{\theta_z}^2(k) G_\theta^T(k) + G_v(k) \sigma_v^2(k) G_v^T(k) \quad (17)$$

where:

- $P_p(k)$ is the estimated covariance matrix at time t_k ;
- $G_\theta = T_c \partial(\mathbf{s}(\theta_z)v_{xu}) / \partial \theta_z |_{[\hat{\theta}_z(k), \hat{v}_{xu}(k)]}$ is the Jacobian matrix with respect to input θ_z computed at $[\hat{\theta}_z(k), \hat{v}_{xu}(k)]$;
- $G_v = T_c \partial(\mathbf{s}(\theta_z)v_{xu} / \partial v_{xu}) |_{[\hat{\theta}_z(k), \hat{v}_{xu}(k)]}$ is the Jacobian matrix with respect to input v_{xu} computed at $[\hat{\theta}_z(k), \hat{v}_{xu}(k)]$;
- $\sigma_{\theta_z}^2(k)$ is the variance of $\hat{\theta}_z(\cdot)$ resulting from the covariance matrix $P_\theta(k)$ of the first EKF at time t_k ;
- $\sigma_v^2(k)$ is the variance of $v_{xu}(\cdot)$ at time t_k .

In the update step, the EKF must rely on the position values collected by some external infrastructure within the reference frame $\langle W \rangle$ defined in Section III-A. Generally, this occurs periodically at a given rate. However, the average update rate can be reduced in particular situations, e.g., when the target does not move or moves very slowly, thus increasing system scalability and autonomy. In the following, a simple update policy is adopted, i.e., time-based with a preset period T_p when the target is detected to be in movement. As a result, the measurement prediction equation can be expressed as

$$\mathbf{c}^+(k+1) = V(k+1) \hat{\mathbf{p}}(k+1) \quad (18)$$

where

$$V(k+1) = \begin{cases} I_2, & (k+1)T_c = iT_p \wedge \hat{\sigma}_{a_{xu}} > \sigma_{a_{\min}} \\ 0_{2,2}, & \text{otherwise} \end{cases} \quad (19)$$

with $i \in \mathbb{Z}$. This means that the sensors of the external infrastructure are queried by the wearable platform only when the boolean condition in (19) is true. If this is not the case, no measurement data are available and the EKF works in open loop. Thus, the Kalman gain associated with (18) when $V(k+1) \neq 0_{2,2}$ (otherwise it is undefined) is given by

$$K_p(k+1) = P_p^+(k+1) V^T(k+1) \cdot [V(k+1) P_p^+(k+1) V^T(k+1) + Q_c(k+1)]^{-1} \quad (20)$$

where $Q_c(k+1)$ is the covariance matrix related to the measured planar coordinates $\bar{\mathbf{c}}(k+1)$. Of course, the elements of $Q_c(k+1)$ depend on the accuracy of the chosen external sensors and on the correlation between the elements of $\bar{\mathbf{c}}(k+1)$ at time t_{k+1} , i.e., $\bar{c}_x(k+1)$ and $\bar{c}_y(k+1)$. Finally, the state update equation and the updated state covariance matrix when $V(k+1) \neq 0_{2,2}$ are given, respectively, by

$$\hat{\mathbf{p}}(k+1) = \mathbf{p}^+(k+1) + K_p(k+1) \bar{\mathbf{c}}(k+1) \quad (21)$$

and

$$P_p(k+1) = [I_2 - K_p(k+1) V(k+1)] P_p^+(k+1) \quad (22)$$

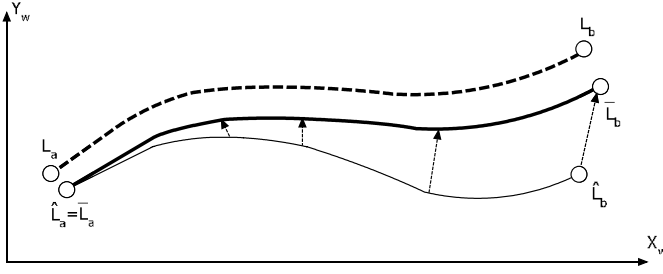


Fig. 4. Qualitative overview of the algorithm for yaw angle estimation. The dashed line between points L_a and L_b represents the actual user trajectory; the thin solid line between \hat{L}_a and \hat{L}_b represents the path estimated by the second EKF; finally, the thick solid line $L_a\bar{L}_b$ shows the trajectory reconstructed using the proposed transformation.

where $\tilde{\mathbf{c}}(k+1) = \bar{\mathbf{c}}(k+1) - \mathbf{c}^+(k+1)$ is the innovation term. On the contrary, when $V(k+1) = 0_{2,2}$ the update step can just rely on the corresponding prediction

$$\begin{aligned}\hat{\mathbf{p}}(k+1) &= \mathbf{p}^+(k+1) \\ P_p(k+1) &= P_p^+(k+1).\end{aligned}\quad (23)$$

E. Yaw Angle Estimation

As stated in Section III-A, yaw angle measurement accuracy is limited by the poor indoor performance of the on-board magnetometer used as a compass. However, the position values collected by the sensors of the external infrastructure can be used to mitigate this problem. The rationale behind the proposed approach is the following: the shape of the user trajectory estimated with the algorithm described in the previous sections is approximately the same as the real one, but with some differences due to the accumulated uncertainty. As a result, when the position values collected by the sensors of the fixed infrastructure are injected into the second EKF, the yaw angle between X_u and X_w can be estimated by minimizing the trajectory deformation from the last adjustment point. Let L_a and L_b be two generic configurations of a given trajectory, shown with the dashed line of Fig. 4. Let \bar{L}_a and \bar{L}_b be the positions measured by the sensors of the fixed infrastructure in L_a and L_b , respectively. If \hat{L}_a and \hat{L}_b represent the corresponding positions estimated by the second EKF, immediately after the external adjustment in L_a (i.e., $\hat{L}_a \approx \bar{L}_a$) and just before receiving the coordinates of point \bar{L}_b , the general idea of the algorithm described in this section is to determine the yaw angle θ_z as if the end of the user trajectory were in \bar{L}_b rather than in \hat{L}_b . With reference to the notation adopted in Section III-D, let $\mathcal{P} = \{\hat{\mathbf{p}}(k-m), \hat{\mathbf{p}}(k-m+1), \dots, \hat{\mathbf{p}}(k)\}$ be the set of user positions estimated by the second EKF between two subsequent adjustments occurred at times $t_{k-m} = (k-m)T_c = (i-1)T_p$ and $t_k = kT_c = iT_p$, respectively. In practice, the elements of \mathcal{P} correspond to the points of the thin solid line in Fig. 4. To compensate for the deformation of the trajectory $\hat{L}_a\hat{L}_b$, while preserving its qualitative shape between \bar{L}_a and \bar{L}_b , a linear stretching algorithm can be used. If $\mathbf{I}(k-m) = \bar{L}_a - \hat{L}_a$ and $\mathbf{I}(k) = \bar{L}_b - \hat{L}_b$ are two planar vectors, each point in \mathcal{P}

undergoes a transformation given by

$$\begin{aligned}\bar{\mathbf{p}}(k-j) &= \hat{\mathbf{p}}(k-j) + \left[\frac{j}{m} \mathbf{I}(k-m) + \frac{m-j}{m} \mathbf{I}(k) \right] \\ &= \hat{\mathbf{p}}(k-j) + \mathbf{I}(k-j).\end{aligned}\quad (24)$$

Notice that $\mathbf{I}(k-j)$ results from the linear combination of the vectors $\mathbf{I}(k-m)$ and $\mathbf{I}(k)$. The elements of the set $\bar{\mathcal{P}} = \{\bar{\mathbf{p}}(k-m), \bar{\mathbf{p}}(k-m+1), \dots, \bar{\mathbf{p}}(k)\}$ correspond to the points of the transformed trajectory, depicted with a thick solid line in Fig. 4. Since the trajectory defined by the points in $\bar{\mathcal{P}}$ has to be compatible with the nonholonomic dynamic given by (15), the following conditions must hold:

$$\bar{\mathbf{p}}(k-j+1) = \bar{\mathbf{p}}(k-j) + s[\bar{\theta}_z(k-j)]\bar{v}_{x_u}(k-j) \quad (25)$$

where $\bar{\theta}_z$ and \bar{v}_{x_u} are the (unknown) yaw angle and user velocity values after trajectory correction and $j = m, m-1, \dots, 0$. Notice that (24) turns to $\bar{\mathbf{p}}(k-m) = \hat{\mathbf{p}}(k-m) + \mathbf{I}(k-m)$ for $j = m$. Therefore, by replacing the discretized version of (15) into (24), it can be easily obtained that

$$\begin{aligned}\bar{\mathbf{p}}(k-j+1) &= \bar{\mathbf{p}}(k-j) + T_c s[\hat{\theta}_z(k-j)]\hat{v}_{x_u}(k-j) \\ &\quad + \frac{1}{m} [\mathbf{I}(k) - \mathbf{I}(k-m)].\end{aligned}\quad (26)$$

Evidently, (25) and (26) can be regarded as equivalent if and only if the second terms of both expressions are the same. In this case, by equating (25) and (26) the values of $\bar{\theta}_z(k-j)$ and $\bar{v}_{x_u}(k-j)$ result from

$$\bar{v}_{x_u}(k-j) = \hat{v}_{x_u}(k-j) \sqrt{1 + f(k, j, m) + h(k, j, m)} \quad (27)$$

$$\bar{\theta}_z(k-j) = \arctan \left[\frac{\Phi(k, j, m)}{\Psi(k, j, m)} \right] \quad (28)$$

where

$$\begin{aligned}f(k, j, m) &= \frac{[\mathbf{I}(k) - \mathbf{I}(k-m)]^T [\mathbf{I}(k) - \mathbf{I}(k-m)]}{[mT_c\hat{v}_{x_u}(k-j)]^2} \\ h(k, j, m) &= \frac{2 \left\{ \cos[\hat{\theta}_z(k-j)] [l_x(k) - l_x(k-m)] \right\}}{mT_c\hat{v}_{x_u}(k-j)} \\ &\quad + \frac{2 \left\{ \sin[\hat{\theta}_z(k-j)] [l_y(k) - l_y(k-m)] \right\}}{mT_c\hat{v}_{x_u}(k-j)}\end{aligned}$$

$$\begin{aligned}\Phi(k, j, m) &= T_c \sin[\hat{\theta}_z(k-j)]\hat{v}_{x_u}(k-j) + \frac{l_y(k) - l_y(k-m)}{m} \\ \Psi(k, j, m) &= T_c \cos[\hat{\theta}_z(k-j)]\hat{v}_{x_u}(k-j) + \frac{l_x(k) - l_x(k-m)}{m}\end{aligned}$$

and $\mathbf{I}(k-m) = [l_x(k-m), l_y(k-m)]^T$. Therefore, by iteratively computing the synthesized inputs derived in (27) and (28) for $\forall j \in \{m, \dots, 0\}$, it is possible to generate a stretched trajectory $\bar{\mathcal{P}}$ that is compatible with the nonholonomic nature of the human motion. The yaw orientation angle to be injected into the first EKF, i.e., $\bar{\eta}_z(k) = \bar{\theta}_z(k)$, is then given by (28) for $j = 0$.

IV. SYSTEM DESCRIPTION

A. Hardware Platform

The algorithm described in Section III was implemented in a custom wearable embedded platform, with dimensions

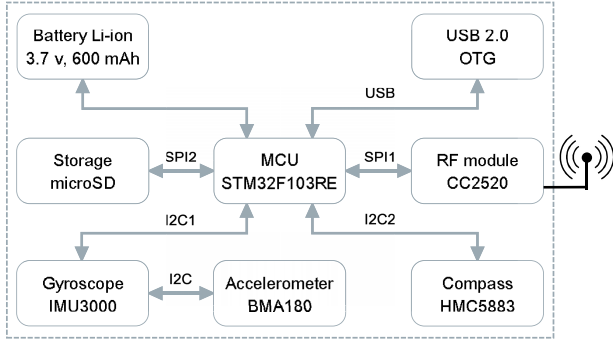


Fig. 5. Block diagram of the wearable embedded platform for user position tracking.

$5.8 \times 3.0 \times 1.9$ cm. The last number refers to the thickness of the system including the battery. The platform was developed in cooperation with Tretec S.r.L., Trento, Italy, and it is endowed with a 32-b ARM Cortex M3 microcontroller (MCU) STM32F103RE running at 72 MHz with 64 kB of RAM and 512 kB of flash memory. The block diagram of the platform is shown in Fig. 5. Wireless communication relies on a radio module TI CC2520 compliant with the Standard IEEE 802.15.4. The set of on-board sensors includes:

- 1) a triaxial accelerometer Bosch BMA180 with a maximum bandwidth of 1.2 kHz, 14 b of resolution and a noise spectral density of $150 \mu\text{g}/\sqrt{\text{Hz}}$;
- 2) a triaxial gyroscope InvenSense IMU3000 with a bandwidth of 8 kHz, 16 b of resolution and a rate noise spectral density of $1.74 \times 10^{-4} \text{ rad/s}/\sqrt{\text{Hz}}$;
- 3) a 12-b triaxial magnetometer Honeywell HMC5883.

All sensors are provided with a digital interface and are connected to the MCU through the I2C bus. In addition, a micro Secure Digital (SD) memory can be used for data logging, thus avoiding slow and power consuming data streaming. The whole platform is powered by a thin 3.7 V, 800 mAh Li-ion battery, rechargeable through a micro USB connector.

The software running on the platform is fully implemented in C language, without any operating system. The communication with the peripherals (sensors, micro SD, and the radio module) is performed through direct memory access and custom interrupt service routines. The on-board RAM is mainly used as a buffer to store data and samples before they are processed by the MCU. With these settings, the algorithms can be executed in real-time at a rate of 250 Hz (when data logging to micro SD is enabled) or 500 Hz (without data logging). In both cases, wireless communication is enabled. Further optimizations might be possible, but the current performance is adequate for the purpose of this paper. One of the main advantages of the developed platform is that the cost of the current prototype (excluding the nonrecurring engineering costs) is indeed in the order of about 100 euros, but it could be considerably reduced if larger volumes of production were considered.

B. Experimental Setup

The position tracking technique was tested on the field in a flat set up by the Trento agency for public housing (ITEA) and

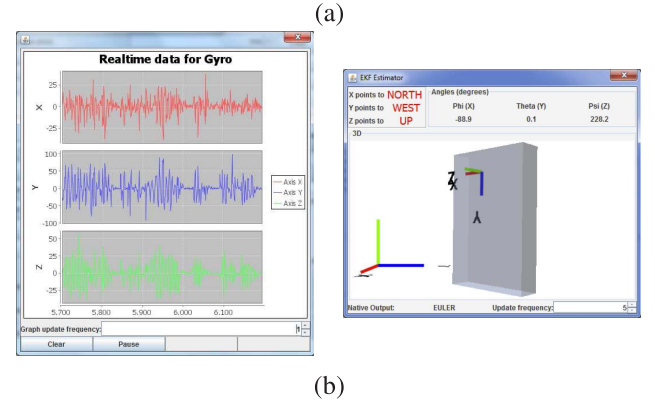
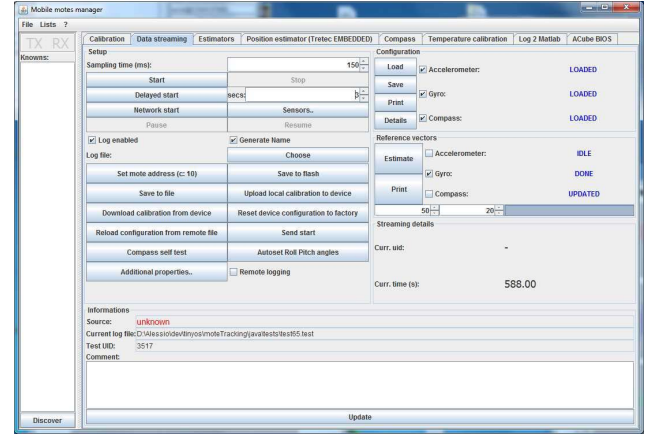


Fig. 6. (a) Screenshots of the Java application for platform control and (b) sensor data acquisition and visualization.

properly instrumented with various sensors, cameras, and other devices for home automation, in the context of the project ACUBE (<http://acube.fbk.eu>). The chosen experimental test-bed is the result of a collaboration between the University of Trento and the research center “Fondazione Bruno Kessler” (FBK). The wearable platform described in Section IV-A was integrated in the existing framework in order to:

- 1) Inject high-accuracy position values into the second EKF with period T_p when the platform is detected to be in movement, as described in Section III-D.
- 2) Build an accurate and fine-grained ground truth to evaluate the accuracy of the proposed solution.

To this purpose, a vision tracking system based on four cameras installed at the corners of the living room was used. Such a system, developed by FBK [50], efficiently uses multiple cameras for tracking different targets and exhibits excellent performance especially in LOS conditions.

An ad hoc Java software application, running on a stand-alone PC, was developed to manage both the embedded platform and the image acquisition process. Using this software, the collected data can be visualized in real-time and/or stored in the PC for further off-line processing and statistical analyses. Some screenshots of this application are shown in Fig. 6(a) and (b). In particular, Fig. 6(a) shows the main window of the software application. It consists of several buttons that can be used to:

- 1) start or handle preliminary platform calibration;
- 2) collect data from different sensors;
- 3) manage system settings;
- 4) configure the external vision system.

Fig. 6(b) shows two examples of windows related to sensor data streaming in real-time. On the left, the angular velocity components measured by the triaxial gyroscope in reference frame $\langle R \rangle$ are plotted in degree/second. On the right, a 3-D box is used to represent the attitude of the embedded platform in $\langle W \rangle$ given by the first EKF.

V. EXPERIMENTAL RESULTS

To evaluate the performance of the proposed localization technique, the embedded platform has to be worn at the user's waist. In fact, in [45] it is shown that the trunk is the best frame to account for the nonholonomic nature of the human locomotion and it also minimizes the unwanted yaw oscillations caused by step alternation. After calibrating both the external vision system and the inertial sensors of the wearable platform, various types of experiments were conducted in the instrumented flat described in Section IV-B. The first set of experiments was mainly conceived to evaluate the performance of the system in terms of accuracy, repeatability, and robustness. For this reason, two very regular, closed, and easily reproducible paths were chosen for testing purposes, i.e., repeated circle-shaped trajectories (Case A) and repeated square-shaped trajectories (Case B), for a total length of 31 and 40 m, respectively.

The second set of experiments was instead focused on a performance evaluation of the platform in more realistic conditions, namely with the user walking naturally over longer piecewise linear trajectories interspersed by some short stops next to some point of interest in the room. In all cases, a user wearing the embedded platform was invited to walk repeatedly along these paths at typical indoor speeds (i.e., between about 1 and 2 m/s). To reduce the intrinsic user uncertainty in repeating the trajectories of Cases A and B, a circle and a square were properly highlighted by some adhesive stickers put on the floor of the living room in known positions of the reference frame $\langle W \rangle$. The origin of $\langle W \rangle$ coincides with one of the corners of the room, with axes X_w and Y_w being approximately parallel to two walls of the room. About 15 identical experiments were repeated in Case A and Case B for different user speeds. The sampling period T_c of the on-board sensors was set to 250 Hz. The camera-based position adjustments were applied to the second EKF at different rates, namely with T_p ranging from 1 to 16 s. Additional images were acquired at a rate of about 30 Hz to track the actual user's position along both X_w and Y_w . The image acquisition latency was properly estimated and compensated in order to align platform- and vision-based position measurement data within a few milliseconds. The EKF parameter values used in all experiments are listed below.

1) First EKF:

$$P_\theta(0) = \text{diag}(0.001, 0.001, 0.001) \text{ rad}^2$$

$$Q_\omega(0) = \text{diag}(0.01, 0.01, 0.01) (\text{rad/s})^2$$

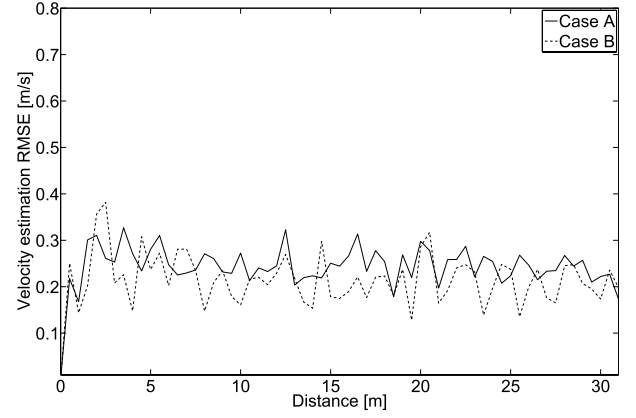


Fig. 7. RMSE of the estimated velocity in Case A and Case B, when the hybrid automaton described in Section III-C is used.

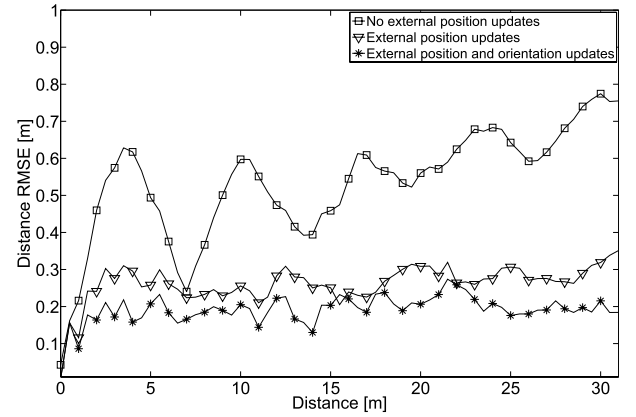


Fig. 8. RMSE patterns of the measured distance as a function of the total traveled distance in Case A, without using external position measures, using external position measures, and using both external position measures and yaw angle estimation.

$$Q_g(0) = \text{diag}(0.24, 0.24, 0.24) (\text{m/s}^2)^2$$

$$Q_n(0) = \text{diag}(7.3 \cdot 10^{-10}, 7.3 \cdot 10^{-10}, 7.3 \cdot 10^{-10})$$

$$Q_\eta(0) = 0.32 \text{ rad}^2.$$

2) Second EKF:

$$P_p(0) = \text{diag}(0.1, 0.1) \text{ m}^2$$

$$Q_c(0) = \text{diag}(0.0025, 0.0025) \text{ m}^2.$$

Fig. 7 shows the root mean square errors (RMSEs) of the estimated user's velocity values, computed over all trajectories of Case A and Case B as a function of the traveled distance. Observe that the RMSE patterns generally fluctuate around 25 cm/s. Such patterns depend not only on the input sensor uncertainty and on the velocity estimation algorithm described in Section III-C, but also on the uncertainty of the method used to determine the real velocity of the user. This is indeed estimated indirectly from the backward Euler difference of subsequent position values measured by the camera. Even if the camera-based absolute position uncertainty is very small, the derivative operator is inherently sensitive to noise and it affects the patterns shown in Fig. 7 by a few centimeters per second. Therefore, we can conclude that the standard

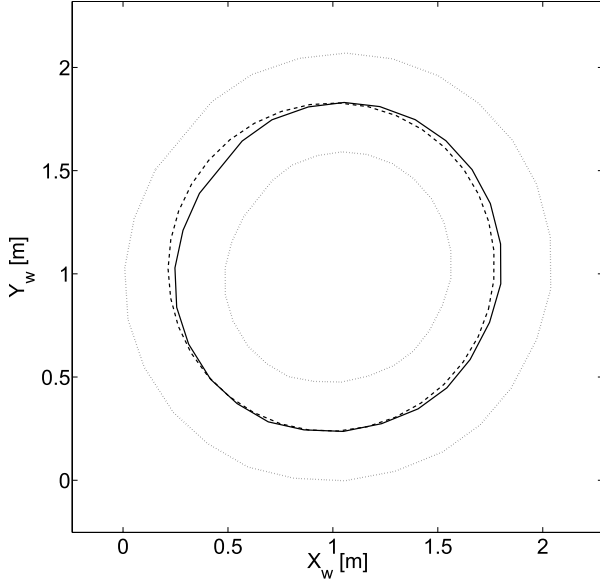


Fig. 9. Average position values estimated by the wearable platform (solid line) along a circular path (dashed line) in Case A. Dotted lines: the $\pm\sigma$ uncertainty boundaries. In this case, external position corrections are repeated every 8 s.

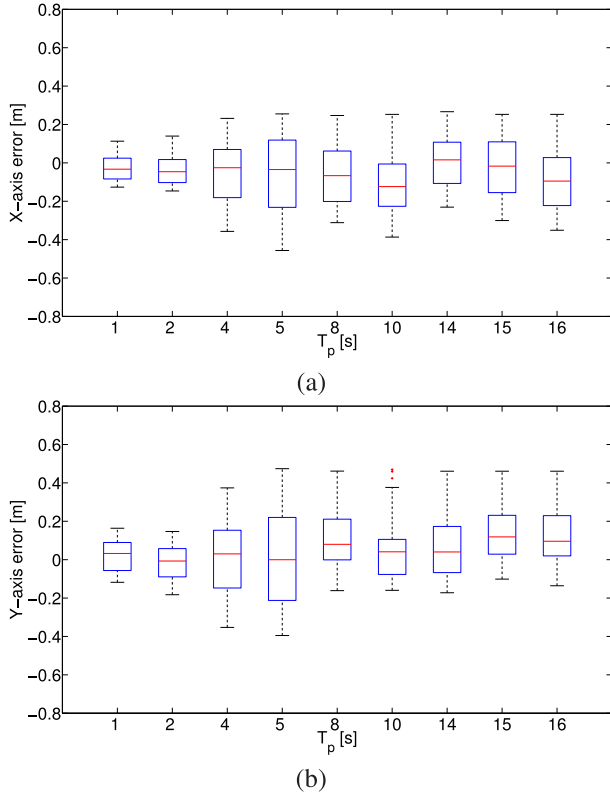


Fig. 10. Box-and-whiskers plots of the position offsets along axes. (a) X_w and (b) Y_w in the case of circular trajectories (Case A). The plots refer to different values of the external update period T_p .

uncertainty associated with \hat{d}_{x_u} alone is certainly a bit smaller than that shown in Fig. 7. More importantly, both RMSE patterns oscillate around constant values, i.e., they do not exhibit relevant drift phenomena as a function of the traveled distance, which instead were observed in [36], where the

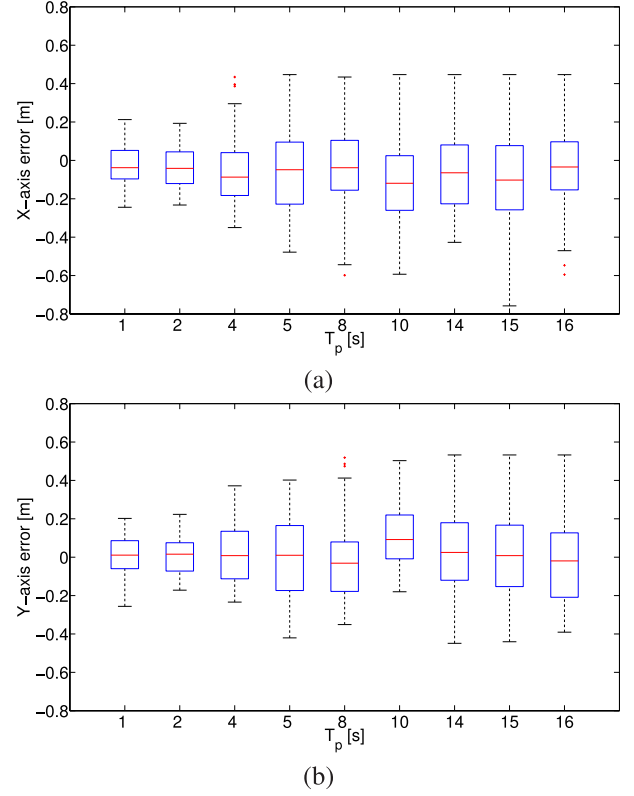


Fig. 11. Box-and-whiskers plots of the position offsets along axes. (a) X_w and (b) Y_w in the case of square-shaped trajectories (Case B). Different plots refer to different values of the external update period T_p .

hybrid automaton described in Section III-C was not used. This implies that the errors in position (obtained from the time integral of the user velocity values) are also much smaller than in [36], when longer observation intervals are considered. Unfortunately, this improvement does not affect yaw angle estimation, which instead is of crucial importance for position tracking accuracy. The effect of the yaw angle estimation algorithm on performance is visible in Fig. 8, where the RMSE patterns of the measured distance are plotted as a function of the total traveled distance in Case A. To better highlight the benefits of the algorithm, the RMSE patterns related to distance estimations in open-loop (i.e., without using external position values) and in closed-loop (i.e., obtained using only the coordinates measured by the vision system with period $T_p = 1$ s) are also reported for comparison. Observe that when the yaw angle estimation technique is used, the RMSE pattern remains steadily below 20 cm even in the long run, whereas in the other cases a growing trend is clearly visible. Similar results are obtained also in Case B.

Fig. 9 summarizes the performance of the proposed localization technique in the case of repeated circles (i.e., Case A) for $T_p = 8$ s. The dashed line highlights the ideal path, whereas the solid line represents the average trajectory estimated over about 15 experiments, consisting of five laps each. The dotted lines refer to the $\pm\sigma$ uncertainty boundaries. The standard uncertainty has been evaluated using a Type-A approach [51], i.e., by computing the average sample standard deviation over all points of the chosen trajectories in which the real position

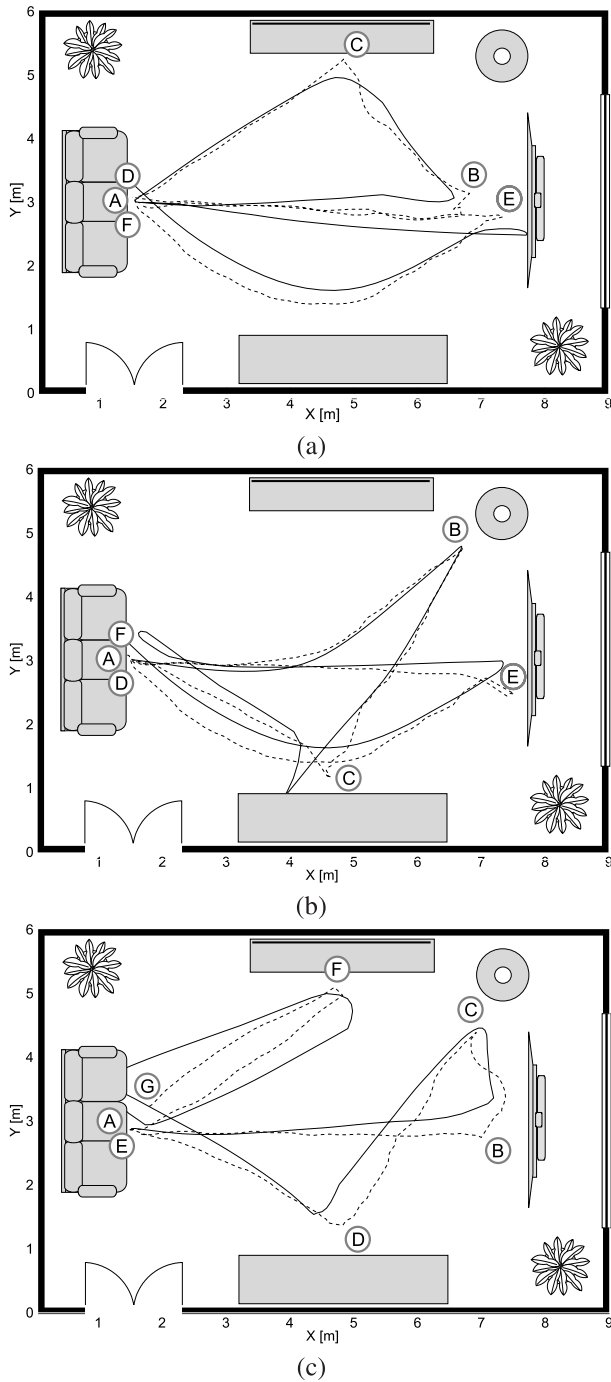


Fig. 12. (a)–(c) Position tracking results along three different natural user trajectories. The path followed by the user and measured by the vision system (dashed line) is compared with the path estimated by the wearable platform (solid line). The user visited in ascending order the waypoints reported in the pictures, starting from point A. At each waypoint, the user stopped for some time (between 1 and 20 s).

was measured by the cameras. Observe that standard uncertainty is about 25 cm. This confirms the good performance of the proposed approach. A more complete performance analysis is reported in Figs. 10(a) and (b) and 11(a) and (b), which show the box-and-whiskers plots of the position offsets with respect to the coordinates measured by the vision system along axes X_w and Y_w , respectively. The boxes refer to different values of the external update period T_p in Case A (Fig. 10) and

Case B (Fig. 11), respectively. Notice that the peak-to-peak errors along both axes are typically smaller than 50 cm and that they are not particularly affected by T_p . Therefore, the system can be autonomous and return reasonable results even if no external updates are available for several seconds. In Case B accuracy is slightly worse, because of the sharp 90-degree rotation angles of the square-shaped path.

The results of some more realistic experiments are shown in Fig. 12. In all of them, the user behavior was quite natural, i.e., moving randomly in the room, stopping occasionally next to some points of interest (e.g., TV set, cabinet, bookcase, lamp, and sofa) and then walking again. In all pictures, the circled letter denote the waypoints where the user stopped for some seconds (between about 1 and 20 s). The ascending order of the letter is related to the direction of motion. The dashed lines refer to the user trajectories measured by the vision system, whereas the solid lines show the trajectories estimated with the proposed technique using the wearable embedded platform and with $T_p = 10$ s. The paths in Fig. 12(a)–(c) are clearly different, but have a comparable duration (between 1 min and 40 s and 2 min). Unfortunately, analyzing the performance in larger spaces is unfeasible at the moment, because the calibrated vision system required to reconstruct the real paths followed by the user are located only in the living room of the flat used for the experimental sessions. Nonetheless, the results in Fig. 12(a)–(c) (along with several others, even longer but too tangled to be read clearly) confirm that the positioning errors along both X_w and Y_w are smaller than ± 50 cm with 97% probability.

VI. CONCLUSION

In this paper, a technique for indoor localization and position tracking of pedestrians is described. The proposed technique relies on multi-sensor data fusion and it is implemented on a wearable embedded platform. User position in a given reference frame is measured mainly through inertial data, by cascading two EKF. The first one estimates the user's attitude in the chosen reference frame, whereas the second EKF returns user's coordinates on a plane. Unlike other solutions described in the literature, the unbounded position uncertainty growth due to the double integration of accelerometer data is mitigated through a heuristic approach that recognizes the steps of the user and removes dynamic velocity estimation drifts. Low-rate position measurements from an external infrastructure (e.g., consisting of camera-based nodes with wireless connectivity) are used to update the state of the second EKF and the yaw angle estimates of the first EKF, to keep positioning uncertainty within specified boundaries. The platform can be worn at the user's waist and can work autonomously with good accuracy (i.e., within about ± 50 cm) for several seconds, without any external intervention. This is beneficial in terms of scalability, since multiple platforms could be worn by different users in the same environment, with no risk of interfering with each other. The proposed technique does not claim to be an ultimate solution to the problem of indoor localization and tracking, but it definitely offers a good tradeoff in terms of accuracy, cost and comfort.

APPENDIX

PROOF OF (2) AND DERIVATION OF $R_{zyx}(\theta)$

Assume that frame $\langle R \rangle$ is subjected to three subsequent rotations, i.e., a rotation by a roll angle θ_x around X_w , a rotation by a pitch angle θ_y around Y_w , and, finally, a rotation by a yaw angle θ_z around Z_w . The three elementary rotation matrices are defined respectively as

$$R_x(\theta_x) = \begin{bmatrix} 1 & 0 & 0 \\ 0 & \cos \theta_x & -\sin \theta_x \\ 0 & \sin \theta_x & \cos \theta_x \end{bmatrix} \quad (\text{A.1})$$

$$R_y(\theta_y) = \begin{bmatrix} \cos \theta_y & 0 & \sin \theta_y \\ 0 & 1 & 0 \\ -\sin \theta_y & 0 & \cos \theta_y \end{bmatrix} \quad (\text{A.2})$$

and

$$R_z(\theta_z) = \begin{bmatrix} \cos \theta_z & -\sin \theta_z & 0 \\ \sin \theta_z & \cos \theta_z & 0 \\ 0 & 0 & 1 \end{bmatrix}. \quad (\text{A.3})$$

As a consequence, the total rotation matrix results from $R_{zyx}(\theta) = R_z(\theta_z) R_y(\theta_y) R_x(\theta_x)$.

The rotation matrix R_{zyx} expresses the relationship between the moving frame $\langle R \rangle$ and the fixed frame $\langle W \rangle$. Hence, it can be also used to define the relation between the angular velocity $\omega = [\omega_x, \omega_y, \omega_z]^T$ and the time derivatives of θ . It is indeed known that the time derivative of a rotation matrix is given by

$$\dot{R}_{zyx}(\theta) = \Omega R_{zyx}(\theta) \quad (\text{A.4})$$

where Ω is the skew symmetric matrix

$$\Omega = \begin{bmatrix} 0 & -\omega_z & \omega_y \\ \omega_z & 0 & -\omega_x \\ -\omega_y & \omega_x & 0 \end{bmatrix} \quad (\text{A.5})$$

accounting for the effect of the angular velocity acting on a rigid body. Therefore, by inverting (A.4) and rearranging the variables it follows that:

$$\Omega = \dot{R}_{zyx}(\theta) R_{zyx}^T(\theta) \Rightarrow \omega = D(\theta) \dot{\theta} \quad (\text{A.6})$$

from which it results that

$$\dot{\theta} = D(\theta)^{-1} \omega. \quad (\text{A.7})$$

Notice that ω is referred to the frame $\langle W \rangle$, while the angular velocities are actually measured in $\langle R \rangle$. If the same procedure is applied to R_{zyx}^T rather than to R_{zyx} , (A.7) can be expressed in the frame $\langle R \rangle$, with $\omega = \omega_r$. Accordingly, (2) is obtained simply by reversing the sign of $D(\theta)^{-1}$, i.e., $E(\theta) = -D(\theta)^{-1}$.

REFERENCES

- [1] N. Bulusu, J. Heidemann, and D. Estrin, "GPS-less low-cost outdoor localization for very small devices," *IEEE Personal Commun.*, vol. 7, no. 5, pp. 28–34, Oct. 2000.
- [2] B. Andó and S. Graziani, "Multisensor strategies to assist blind people: A clear-path indicator," *IEEE Trans. Instrum. Meas.*, vol. 58, no. 8, pp. 2488–2494, Aug. 2009.
- [3] Y. Gu, A. Lo, and I. Niemegeers, "A survey of indoor positioning systems for wireless personal networks," *IEEE Commun. Surveys Tuts.*, vol. 11, no. 1, pp. 13–32, Mar. 2009.
- [4] H. Liu, H. Darabi, P. Banerjee, and J. Liu, "Survey of wireless indoor positioning techniques and systems," *IEEE Trans. Syst., Man, Cybern., C, Appl. Rev.*, vol. 37, no. 6, pp. 1067–1080, Nov. 2007.
- [5] L. Angrisani, A. Baccigalupi, and R. Schiano Lo Moriello, "Ultrasonic time-of-flight estimation through unscented Kalman filter," *IEEE Trans. Instrum. Meas.*, vol. 55, no. 4, pp. 1077–1084, Aug. 2006.
- [6] E. Aitenbichler and M. Mühlhäuser, "An IR local positioning system for smart items and devices," in *Proc. 23rd ICDCS*, Providence, NJ, USA, May 2003, pp. 334–339.
- [7] D. Glas, T. Miyashita, H. Ishiguro, and N. Hagita, "Laser-based tracking of human position and orientation using parametric shape modeling," *Adv. Robot.*, vol. 23, no. 4, pp. 405–428, 2009.
- [8] C. X. Dai, Y. F. Zheng, and X. Li, "Pedestrian detection and tracking in infrared imagery using shape and appearance," *Comput. Vis. Image Understand.*, vol. 106, nos. 2–3, pp. 288–299, May 2007.
- [9] F. Chavand, E. Colle, Y. Chekhar, and E. N'zi, "3-D measurements using a video camera and a range finder," *IEEE Trans. Instrum. Meas.*, vol. 46, no. 6, pp. 1229–1235, Dec. 1997.
- [10] P. Vadakkepat and L. Jing, "Improved particle filter in sensor fusion for tracking randomly moving object," *IEEE Trans. Instrum. Meas.*, vol. 55, no. 5, pp. 1823–1832, Oct. 2006.
- [11] G. Oberholzer, P. Sommer, and R. Wattenhofer, "Spiderbat: Augmenting wireless sensor networks with distance and angle information," in *Proc. Int. Conf. IPSN*, Chicago, IL, USA, Apr. 2011, pp. 211–222.
- [12] B. Ando, S. Baglio, S. La Malfa, A. Pistorio, and C. Trigona, "A smart wireless sensor network for AAL," in *Proc. IEEE Int. Workshop M&N*, Anacapri, Italy, Oct. 2011, pp. 122–125.
- [13] A. Harter and A. Hopper, "A distributed location system for the active office," *IEEE Netw.*, vol. 8, no. 1, pp. 62–70, Jan./Feb. 1994.
- [14] (2008). *Firefly Motion Capture System* [Online]. Available: <http://www.cybernet.com/interactive/firefly/index.html>
- [15] Y. Hada and K. Takase, "Multiple mobile robot navigation using the indoor global positioning system (iGPS)," in *Proc. IEEE/RSJ Int. Conf. Intell. Robots Syst.*, vol. 2, Oct./Nov. 2001, pp. 1005–1010.
- [16] E. Lobaton, R. Vasudevan, R. Bajcsy, and S. Sastry, "A distributed topological camera network representation for tracking applications," *IEEE Trans. Image Process.*, vol. 19, no. 10, pp. 2516–2529, Oct. 2010.
- [17] T. S. Rappaport, *Wireless Communications—Principles and Practice*. Upper Saddle River, NJ, USA: Prentice-Hall, 1996.
- [18] A. Cesare and V. Giovanni, "A RSSI-based and calibrated centralized localization technique for wireless sensor networks," in *Proc. Int. Conf. Pervas. Comput. Commun.*, Mar. 2006, pp. 301–305.
- [19] H. Liu, H. Darabi, P. Banerjee, and J. Liu, "Survey of wireless indoor positioning techniques and systems," *IEEE Trans. Syst. Man, Cybern., C, Appl. Rev.*, vol. 37, no. 6, pp. 1067–1080, Nov. 2007.
- [20] H. Chen, Q. Shi, R. Tan, H. Poor, and K. Sezaki, "Mobile element assisted cooperative localization for wireless sensor networks with obstacles," *IEEE Trans. Wireless Commun.*, vol. 9, no. 3, pp. 956–963, Mar. 2010.
- [21] D. Lymberopoulos, Q. Lindsey, and A. Savvides, "An empirical characterization of radio signal strength variability in 3-D IEEE 802.15.4 networks using monopole antennas," in *Wireless Sensor Networks* (Lecture Notes in Computer Science), vol. 3868. Berlin-Heidelberg, Germany: Springer-Verlag, 2006, pp. 326–341.
- [22] P. Pivato, L. Palopoli, and D. Petri, "Accuracy of RSS-based centroid localization algorithms in an indoor environment," *IEEE Trans. Instrum. Meas.*, vol. 60, no. 10, pp. 3451–3460, Oct. 2011.
- [23] D. Macii, A. Colombo, P. Pivato, and D. Fontanelli, "A data fusion technique for wireless ranging performance improvement," *IEEE Trans. Instrum. Meas.*, vol. 62, no. 1, pp. 27–37, Jan. 2013.
- [24] G. Santinelli, R. Giglietti, and A. Moschitta, "Self-calibrating indoor positioning system based on ZigBee devices," in *Proc. IEEE Instrum. Meas. Technol. Conf.*, Singapore, May 2009, pp. 1205–1210.
- [25] A. De Angelis, M. Dionigi, A. Moschitta, and P. Carbone, "A low-cost ultra-wideband indoor ranging system," *IEEE Trans. Instrum. Meas.*, vol. 58, no. 12, pp. 3935–3942, Dec. 2009.
- [26] D. Dardari, A. Conti, U. Ferner, A. Giorgetti, and M. Win, "Ranging with ultrawide bandwidth signals in multipath environments," *Proc. IEEE*, vol. 97, no. 2, pp. 404–426, Feb. 2009.
- [27] A. Sikora and V. Groza, "Fields tests for ranging and localization with time-of-flight-measurements using chirp spread spectrum RF-devices," in *Proc. IEEE IMTC*, Warsaw, Poland, May 2007, pp. 1–6.
- [28] C. De Dominicis, P. Pivato, P. Ferrari, D. Macii, E. Sisinni, and A. Flammini, "Timestamping of IEEE 802.15.4a CSS signals for wireless ranging and time synchronization," *IEEE Trans. Instrum. Meas.*, vol. 62, no. 8, pp. 2286–2296, Aug. 2013.
- [29] G. Lachapelle, "GNSS indoor location technologies," *J. Global Posit. Syst.*, vol. 3, nos. 1–2, pp. 2–11, 2004.

- [30] A. Wieser, "High-sensitivity GNSS: The trade-off between availability and accuracy," in *Proc. 3rd Symp. Geodesy Geotech. Struct. Eng./12th Symp. Deformat. Meas.*, 2006, pp. 1–12.
- [31] M. Choudhury, C. Rizos, and B. Harvey, "A survey of techniques and algorithms in deformation monitoring applications and the use of the Locata technology for such applications," in *Proc. 22nd Int. Technol. Meeting Satellite Division Inst. Navigat.*, Savannah, GA, USA, 2009, pp. 22–25.
- [32] J. Barnes, C. Rizos, A. Pahwa, N. Politi, and J. V. Cranenbroeck, "The potential for Locata technology for structural monitoring applications," *J. Global Posit. Syst.*, vol. 6, no. 2, pp. 166–172, 2007.
- [33] J. Barnes, C. Rizos, M. Kanli, D. Small, G. Voigt, N. Gambale, et al., "Structural deformation monitoring using Locata," in *Proc. 1st FIG Int. Symp. Eng. Surveys Construct. Works Struct. Eng.*, 2004, pp. 1–16.
- [34] M. Narins, L. Eldredge, P. Enge, M. Harrison, R. Kenagy, and S. Lo, "Alternative position, navigation, and timing—the need for robust radionavigation," in *Proc. Global Navigat. Satellite Syst., Rep. Joint Workshop Nat. Acad. Eng. Chin. Acad. Eng.*, 2012, pp. 119–135.
- [35] B. Barshan and H. Durrant-Whyte, "Inertial navigation systems for mobile robots," *IEEE Trans. Robot. Autom.*, vol. 11, no. 3, pp. 328–342, Jun. 1995.
- [36] A. Colombo, D. Fontanelli, D. Macii, and L. Palopoli, "A wearable embedded inertial platform with wireless connectivity for indoor position tracking," in *Proc. Int. Instrum. Meas. Technol. Conf.*, Hangzhou, China, May 2011, pp. 1518–1523.
- [37] B. Barshan and H. Durrant-Whyte, "Evaluation of a solid-state gyroscope for robotics applications," *IEEE Trans. Instrum. Meas.*, vol. 44, no. 1, pp. 61–67, Feb. 1995.
- [38] G. Pang and H. Liu, "Evaluation of a low-cost MEMS accelerometer for distance measurement," *J. Intell. Robot. Syst.*, vol. 30, no. 3, pp. 249–265, Mar. 2001.
- [39] F. Cavallo, A. M. Sabatini, and V. Genovese, "A step toward GPS/INS personal navigation systems: Real-time assessment of gait by foot inertial sensing," in *Proc. IEEE/RSJ Int. Conf. IROS*, Aug. 2005, pp. 1187–1191.
- [40] P. Coronel, S. Furrer, W. Schott, and B. Weiss, "Indoor location tracking using inertial navigation sensors and radio beacons," in *Proc. 1st Int. Conf. IOT*, vol. 4952, Mar. 2008, pp. 325–340.
- [41] L. Klingbeil, M. Romanovas, P. Schneider, M. Traechtler, and Y. Manoli, "A modular and mobile system for indoor localization," in *Proc. Int. Conf. IPIN*, Zurich, Switzerland, Sep. 2010, pp. 1–10.
- [42] E. Foxlin, "Pedestrian tracking with shoe-mounted inertial sensors," *IEEE Comput. Graph. Appl.*, vol. 25, no. 6, pp. 38–46, Nov./Dec. 2005.
- [43] A. Jimenez, F. Seco, J. Prieto, and J. Guevara, "Indoor pedestrian navigation using an INS/EKF framework for yaw drift reduction and a foot-mounted IMU," in *Proc. WPNC*, Dresden, Germany, Mar. 2010, pp. 135–143.
- [44] K. Abdulrahim, C. Hide, T. Moore, and C. Hill, "Aiding MEMS IMU with building heading for indoor pedestrian navigation," in *Proc. UPINLBS*, Kirkkonummi, Finland, Oct. 2010, pp. 1–6.
- [45] G. Arechavaleta, J.-P. Laumond, H. Hicheur, and A. Berthoz, "On the nonholonomic nature of human locomotion," *Auto. Robots*, vol. 25, nos. 1–2, pp. 25–35, Aug. 2008.
- [46] N. Piatto, N. Conci, and F. De Natale, "Syntactic matching of trajectories for ambient intelligence applications," *IEEE Trans. Multimedia*, vol. 11, no. 7, pp. 1266–1275, Nov. 2009.
- [47] K. D. Frampton, "Acoustic self-localization in a distributed sensor network," *IEEE Sensors J.*, vol. 6, no. 1, pp. 166–172, Feb. 2006.
- [48] V. Cevher and L. M. Kaplan, "Acoustic sensor network design for position estimation," *ACM Trans. Sensor Netw.*, vol. 5, no. 3, pp. 1–28, May 2009.
- [49] S. Sprager and D. Zazula, "A cumulant-based method for gait identification using accelerometer data with principal component analysis and support vector machine," *WSEAS Trans. Signal Process.*, vol. 5, pp. 369–378, Nov. 2009.
- [50] O. Lanz, "Approximate Bayesian multibody tracking," *IEEE Trans. Pattern Anal. Mach. Intell.*, vol. 28, no. 9, pp. 1436–1449, Sep. 2006.
- [51] *Evaluation of Measurement Data – Guide to the Expression of Uncertainty in Measurement*, JCGM, Geneva, Switzerland, 2008.



Alessio Colombo (S'07) received the B.S. and M.S. degrees in computer science from the University of Trento, Trento, Italy, in 2007 and 2010, respectively, where he has been pursuing the Ph.D. degree in information technologies and computer science with the Department of Information Engineering and Computer Science since 2010.

He was a Visiting Researcher with the National Institute for Research in Computer Science and Control, Rennes, France, in 2012. His current research interests include embedded system control and design, indoor localization, and motion planning algorithms for autonomous robots in crowded environments.



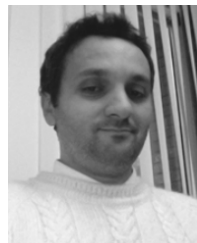
Daniele Fontanelli (M'10) received the M.S. degree in information engineering and the Ph.D. degree in automation, robotics, and bioengineering from the University of Pisa, Pisa, Italy, in 2001 and 2006, respectively.

He was a Visiting Scientist with the Vision Laboratory, University of California at Los Angeles, Los Angeles, CA, USA, from 2006 to 2007. From 2007 to 2008, he was an Associate Researcher with the Interdepartment Research Center E. Piaggio, University of Pisa. In 2008, he was an Associate Researcher with the Department of Information Engineering and Computer Science, University of Trento, Trento, Italy. His current research interests include real-time control and estimation, resource aware control, mobile robotics and visual serving, localization algorithms, human-robot interaction, and wireless sensor networks.



David Macii (M'06) received the Ph.D. degree in information engineering from the University of Perugia, Perugia, Italy, in 2003.

He was involved in research in various institutions, particularly with the Department of Digital Networks, German Aerospace Center, Munich, Germany, in 2000, the Applied DSP and VLSI Research Group, University of Westminster, London, U.K., in 2002, the Advanced Learning and Research Institute, University of Lugano, Lugano, Switzerland, from 2003 to 2005, and the Berkeley Wireless Research Center, University of California at Berkeley, Berkeley, CA, USA, from 2009 to 2010, as a Fulbright Research Scholar. He is currently an Assistant Professor with the Department of Industrial Engineering, University of Trento, Trento, Italy. His current research interests include design, implementation, and characterization of embedded systems, with a special emphasis on power reduction and estimation techniques, distributed synchronization, and wireless sensor networks.



Luigi Palopoli (M'02) received the M.S. degree in computer engineering from the University of Pisa, Pisa, Italy, and the Ph.D. degree in computer engineering from Scuola Superiore Sant'Anna, Pisa, in 2002 and 1992, respectively.

He is an Associate Professor of computer engineering with the University of Trento, Trento, Italy. His current research interests include embedded system design with a particular focus on resource-aware control design and adaptive mechanisms for QoS management.

Dr. Palopoli has served on the Program Committees of different conferences in the area of real-time and control systems.